OPEN ACCESS

Energy Storage ARTICLE

The Innovation Energy

Unusual fullerene-like curved surface with unique Fe-N_4 sites for highly efficient oxygen reduction reaction in zinc-air battery

Shaohuan Hong,[1] Lingjie Yuan,[2] Shenglin Liu,[1] Kai Zhang,[1] Rui Xiao,[1] Yonglian Xiong,[4] Hualin Ye,[3,*] Yinlong Zhu,[2,*] and Feng Gong[1,*]

*Correspondence: gongfeng@seu.edu.cn (F.G.); zhuyl1989@nuaa.edu.cn (Y.Z.); hualin@njnu.edu.cn (H.Y.).

Received: November 12, 2025; Accepted: March 9, 2026; Published Online: April 20, 2026; https://doi.org/10.59717/j.xinn-energy.2026.100154

GRAPHICAL ABSTRACT

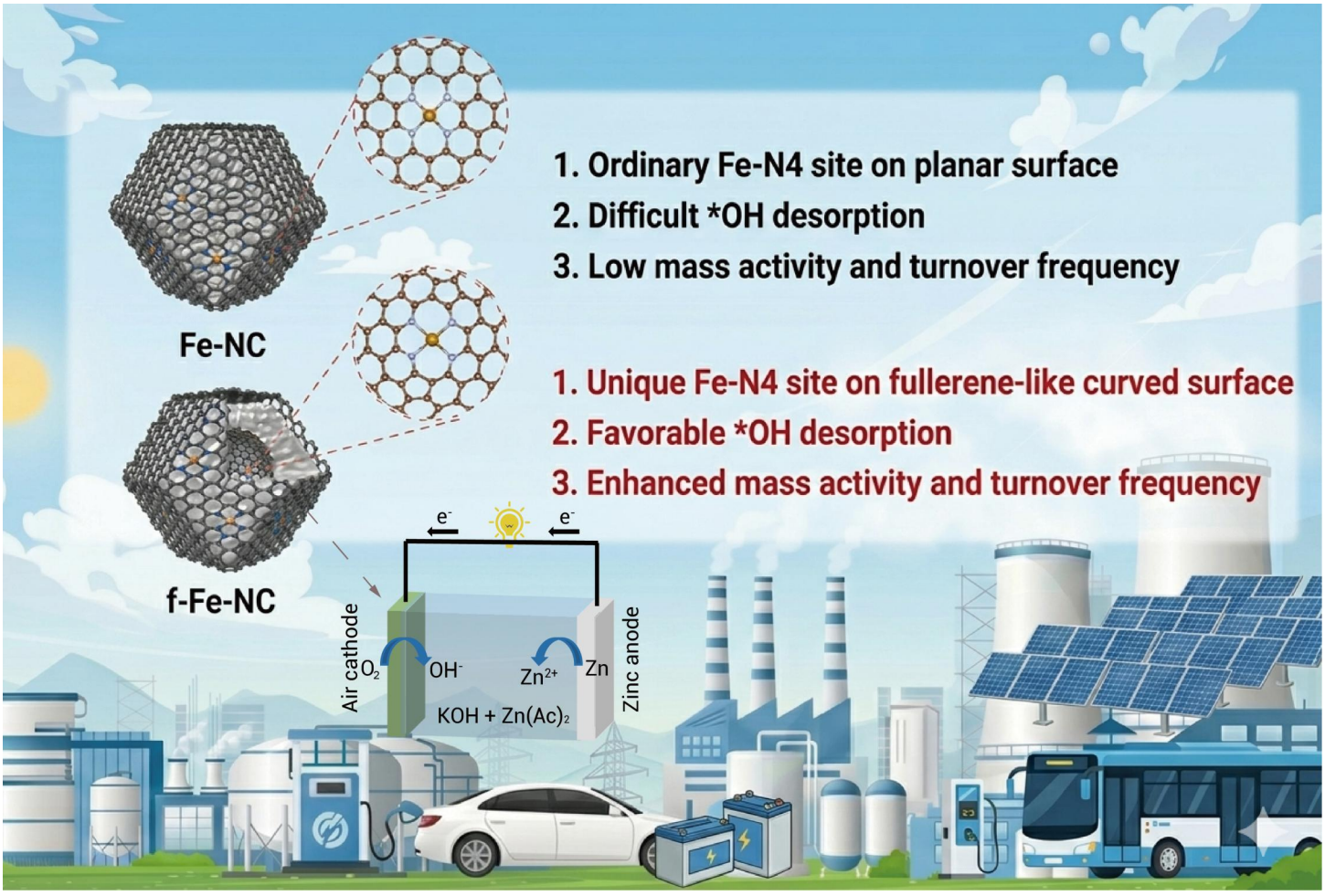

PUBLIC SUMMARY

- A composite-template strategy creates Fe–N–C catalysts with curved Fe–N_4 sites and hierarchical porosity.
- Curved surfaces stretch Fe–N bonds, promoting *OH desorption and accelerating ORR kinetics.
- The catalyst achieves a high half-wave potential of 0.91 V and ~7× higher mass activity.
- Calculations show a lower rate-determining barrier and weakened Fe–OH bonding.
- In Zn–air batteries, it outperforms Pt/C with higher power density and capacity.

ARTICLE Energy Storage

www.the-innovation.org/the-innovation-energy

Unusual fullerene-like curved surface with unique Fe-N_4 sites for highly efficient oxygen reduction reaction in zinc-air battery

Shaohuan Hong,[1] Lingjie Yuan,[2] Shenglin Liu,[1] Kai Zhang,[1] Rui Xiao,[1] Yonglian Xiong,[4] Hualin Ye,[3,*] Yinlong Zhu,[2,*] and Feng Gong[1,*]

[1]Key Laboratory of Energy Thermal Conversion and Control of Ministry of Education, School of Energy and Environment, Southeast University, Nanjing 211189, China

[2]Institute for Frontier Science, Nanjing University of Aeronautics and Astronautics, Nanjing 210016, China

[3]Jiangsu Key Laboratory of New Power Batteries, Jiangsu Collaborative Innovation Center of Biomedical Functional Materials, School of Chemistry and Materials Science, Nanjing Normal University, Nanjing 210023, China

[4]College of Automotive Engineering, Yancheng Institute of Technology, Yancheng 224051, China

*Correspondence: gongfeng@seu.edu.cn (F.G.); zhuyl1989@nuaa.edu.cn (Y.Z.); hualin@njnu.edu.cn (H.Y.).

Received: November 12, 2025; Accepted: March 9, 2026; Published Online: April 20, 2026; https://doi.org/10.59717/j.xinn-energy.2026.100154

Citation: Hong S., Yuan L., Liu S., et al. (2026). Unusual fullerene-like curved surface with unique Fe-N_4 sites for highly efficient oxygen reduction reaction in zinc-air battery. *The Innovation Energy* **3**:100154.

Iron-Nitrogen-carbon (Fe-N-C) catalysts are promising substitutes for Pt-based catalysts in oxygen reduction reaction (ORR) for zinc-air battery. However, the sluggish kinetics of ORR on conventional Fe-N-C catalysts resulted from difficult desorption of *OH intermediate and the slow mass transfer significantly impede their practical application. Herein, a novel composite template-assisted strategy is proposed to prepare Fe-N_4 sites on unusual fullerene-like curved surface featuring stretched Fe-N bonds and hierarchically porous structure (denoted as f-Fe-NC). With unique curved Fe-N_4 sites and hierarchical porosity, f-Fe-NC exhibits an impressive half-wave potential ($E_{1/2}$) of 0.91 V vs. RHE. Moreover, the mass activity of f-Fe-NC is nearly sevenfold of that of ordinary Fe-NC featuring planar Fe-N_4 sites and microporous structure, and the turnover frequency of f-Fe-NC increases at exponent level compared to ordinary Fe-NC. Theoretical calculations demonstrate the reduced energy barrier of rate-determining step and favorable *OH desorption on f-Fe-NC because of the degradation of bond order of Fe-OH bond. Zinc-air battery based on f-Fe-NC exhibits a power density of 182 mW cm^{-2} and a specific capacity of 811 mAh g^{-1} at 10 mA cm^{-2}, overtaking those of commercial Pt/C. Our study opens a new avenue for the rational design of electrochemically and structurally advanced ORR catalysts.

Introduction

Zinc-air battery (ZAB) has been commonly considered as an ideal alternative for the next-generation energy conversion technology owing to its high specific capacity, nonflammability and eco-friendliness.[1] As the basic cathodic process in ZAB, oxygen reduction reaction (ORR) plays a vital role in the development of this sustainable energy device. Currently, platinum group metal (PGM) catalysts are widely used in the air cathode of ZABs owing to their excellent performance and stability in alkaline ORR.[2] However, the scarcity and high price of Pt dramatically increase the production costs of ZABs, which hampers their large-scale application. Consequently, it is necessary to develop cost-effective non-PGM catalysts with efficient electrocatalytic activity.[3]

Fe and N co-doped carbon with atomically dispersed Fe single atom (Fe-N-C) has demonstrated remarkable performance towards ORR in recent studies,[4] which has been considered as one of the most promising alternatives to PGM catalysts due to its low cost, ultrahigh atom utilization efficiency and tunable coordination environment.[5] The ORR process in ZABs on Fe-N-C catalysts consists of four proton-coupled electron transfer steps: 1) $*O_2 + H_2O + e^- \rightarrow *OOH + OH^-$, 2) $*OOH + e^- \rightarrow *O + OH^-$, 3) $*O + H_2O + e^- \rightarrow *OH + OH^-$ and 4) $*OH + e^- \rightarrow * + OH^-$. Previous studies have proven that the fourth step, namely, the desorption of *OH intermediate is the rate-determining step, due to the strong interaction between the symmetric square-planar Fe-N_4 site and *OH intermediate.[6,7] The coordination between Fe atoms and strongly electronegative N atoms is unfavorable for the efficient turnover of oxygenated intermediates in ORR process.[8–10] Currently, some effective solutions to this problem are creating asymmetric coordination environment by replacing several N atoms with heteroatoms like P, S and O[11–13] or inducing an extra metallic active site to form dual-atom active center.[14,15] These solutions are intended to regulate the electronic structure of Fe single atom to facilitate the desorption of *OH intermediate. Except from these strategies, previous studies[16,17] have also demonstrated the Fe single atoms on curved surface with optimized electronic structure are beneficial for the dynamic generation and desorption of ORR intermediates, as the stretched Fe-N bond in curved surface can effectively modulate the adsorption energy of each ORR intermediate to achieve lower overpotential.

On the other hand, most of current Fe-N-C catalysts are derived from metal-organic framework (MOF) and zeolitic imidazolate framework (ZIF) by pyrolysis,[18] which are dominated by the microporous structure. The micropores structural feature often leads to hindered mass transfer and lowers the atom utilization efficiency,[19] thereby resulting in the sluggish ORR kinetics, and ultimately limiting the practical performance of ZAB and PEMFC. In recent studies,[20–23] hierarchically porous structure containing both micropores and mesopores has been demonstrated to be favorable for enhancing the ORR kinetics, as mesopores promote mass transfer and micropores ensure a high density of active sites. Therefore, there is an urgent need to accelerate the desorption of *OH intermediates, boost the mass transfer and improve the atom utilization efficiency simultaneously to achieve optimal ORR activity. However, simultaneous preparation of highly active Fe single atom sites and hierarchically porous structures remains a challenge.

Here, we report a composite template-assisted strategy to synthesize Fe-N_4 sites on fullerene-like curved surface with hierarchically porous structure (f-Fe-NC). By performing a series of characterizations, including X-ray diffraction (XRD), Aberration-corrected TEM (AC-TEM), electron paramagnetic resonance (EPR), and Raman spectra, the existence of massive number of carbon pentagons has been firmly demonstrated, while no extra carbon vacancies with unpaired electrons are observed, indicating the formation of fullerene-like curved surface. The synchrotron-radiation-based X-ray absorption near-edge structure (XANES) and extended X-ray absorption fine structure (EXAFS) fitting further confirm the existence of Fe-N_4 sites in f-Fe-NC with elongated Fe-N bond and the carbon pentagons are adjacent to Fe-N_4 sites. The stretched Fe-N bonds and hierarchically porous structure endow f-Fe-NC with excellent ORR performance, achieving a high half wave potential ($E_{1/2}$) of 0.91 V in alkaline media and exponentially increasing mass activity (MA) and turnover frequency (TOF) compared to ordinary Fe-NC. Theoretical calculations reveal the rearranged electronic structure of Fe atom caused by carbon pentagons, which facilitates the desorption of *OH intermediate. Moreover, aqueous zinc-air battery based on f-Fe-NC achieve an impressive electrochemical performance with a peak power density of 182 mW cm^{-2} and a specific capacity of 811 mAh g^{-1}, implying its potential for practical application.

MATERIALS AND METHODS

All the chemical reagents were used as purchased without further treatment. Zinc nitrate hexahydrate ($Zn(NO_3)_2{\cdot}6H_2O$) and 2-methylimidazole (2-MIeM) were purchased from Shanghai Aladdin Biochemical Technology Co., Ltd. Zinc oxide (ZnO, 30 ± 10 nm), Dopamine hydrochloride and Tris-HCl buffer (10 mM, pH=8.5) were purchased from Meryer (Shanghai) Chemical Technology Co.,Ltd. Iron (II) phthalocyanine were purchased from Shanghai Macklin Biochemical Co.,Ltd.

Synthesis of f-Fe-NC

0.4 g ZnO (30 nm) was added to 200 ml Tris-HCl buffer and stirred for 30 min at 25 °C to obtain a well-mixed suspension. Subsequently, 0.2 g dopamine hydrochloride was added into the solution, and the solution was stirred for 24 h at 25 °C. Finally, the black precipitates were collected by centrifuging, washed with deionized water for several times and dried in a vacuum oven at 80 °C for 8 h to obtain PDA@ZnO sphere (PZS) templates. Subsequently, PZS templates and 1.57 g $Zn(NO_3)_2{\cdot}6H_2O$ were added into 40 ml methanol. The mixture was ultrasonicated for 30 min to form a well-mixed suspension (denoted as solution A). After that, 20 ml DMF containing 30 mg Iron (II) phthalocyanine (FePc) was added into solution A and the solution was stirred for 10 min at 60 °C. 1.75 g 2-MIeM was dissolved in 40 ml methanol and stirred for 10 min to form a clear solution (denoted as solution B). Then, solution B was injected into solution A and kept stirring for 24 h at 60 °C. The precipitate was collected by centrifuging, washed with methanol for several times and dried in a vacuum oven at 60 °C for 8 h to obtain FePc-ZIF-8@PZS. Finally, 0.2 g FePc-ZIF-8@PZS was carbonized at 1000 °C for 2 h under Ar atmosphere with a heating rate of 10 °C/min. The obtained black powder was washed with 1 M HCl and deionized water, and dried in vacuum. The resulting black powder was heated again at 1000 °C for 1 h under Ar atmosphere with a heating rate of 10 °C/min to obtain f-Fe-NC.

Synthesis of Fe-NC

The Fe-NC was synthesized following the same process as the synthesis of f-Fe-NC, except that PZS templates were not added into solution A.

Synthesis of f-NC

The f-NC was syntheszed following the same process as the synthesis of f-Fe-NC, except that FePc were not added into solution A.

More experimental details can be found in Supporting Information.

Result and discussion

Synthesis and characterization

A composite template-assisted strategy was developed to synthesize Fe-N_4 sites on fullerene-like surface, as shown in Figure 1A. Firstly, nanoparticles ZnO (d=30 ± 10 nm) were coated with a thin polydopamine (PDA) layer by the self-polymerization effect between hydrolyzed Zn^{2+} and dopamine hydrochloride in the Tris-HCl buffer to form PDA@ZnO spheres (PZS) template (Figure S1).[24] Subsequently, the PZS template, $Zn(NO_3)_2{\cdot}6H_2O$, 2-MIeM and FePc were dispersed in methanol at 60°C. During the self-assembly, the PDA layer would generate abundant -NH_2 species on its surface to congregate Zn^{2+} and FePc,[25] which would further coordinate with 2-MIem to form FePc-ZIF-8@PZS. FePc-ZIF-8 was synthesized without PZS template as the precursor of Fe-N_4 site on planar surface. Scanning electron microscopy (SEM) images and X-ray diffraction (XRD) were conducted to confirm the self-assembly of FePc-ZIF-8 and PZS template. As shown in SEM images (Figure S2), the average diameter of dodecahedral FePc-ZIF-8@PZS is 376 nm, while that of FePc-ZIF-8 is only 277 nm, demonstrating the PZS templates are well embedded into the imidazole framework. The XRD patterns (Figure S3) of FePc-ZIF-8@PZS and FePc-ZIF-8 align well with that of the simulated ZIF-8 pattern, signifying that the PZS template and FePc have not disordered the crystalline integrity of ZIF-8.

The FePc-ZIF-8@PZS precursor was subjected to carbonization under Ar atmosphere at 1000 °C. During the pyrolysis, ZnO in the composite template would react with the carbon matrix to form Zn and carbon defects.[26] Meanwhile, Zn species would evaporate at 1000 °C, leaving a substantial number of hollow structures. Those internal hollow structures can cause shrinkage stress and inward collapse, thus generating the curved surface on carbon matrix. Then, the obtained black powder was washed by HCl and subjected to secondary pyrolysis to remove the residual ZnO and Zn to achieve f-Fe-NC. For comparison, planar Fe-NC catalyst and nitrogen-doped carbon with carbon pentagons (denoted as f-NC) were synthesized through the same pyrolysis procedure by using the FePc-ZIF-8 and ZIF-8@PZS as the precursor, respectively.

SEM and transmission electron microscopy (TEM) images (Figures 1B&C) reveal that the f-Fe-NC is featured with curved and wrinkled edges, and numerous bright spots (highlighted by red cycles in Figure 1C), which are identified as the hollow structure formed from the removal of composite template. Conversely, the Fe-NC inherits the dodecahedral structure with flat surface from the precursor (Figure S4A&B). The unique morphology of f-Fe-NC demonstrates the strong interaction between the carbon framework and the composite templates, causing inward collapse and lattice strain. The XRD patterns of two samples (Figure 1D) display two peaks at ~ 26° and 44°, corresponding to the (002) and (101) facets of graphitic carbon, respectively.[27] Notably, the (002) peak of f-Fe-NC is shifted positively compared with that of Fe-NC, indicating a decrease of interplanar spacing[28] resulted from the inward collapse and lattice strain, demonstrating the presence of curved carbon surface. Besides, no peaks related to Fe impurity phase are detected in XRD patterns, indicating the absence of metallic Fe or oxides of Fe. Element mapping images (Figure 1E and Figure S4C) also confirm the homogeneous distribution of each element in these two catalysts. The Aberration-corrected high-angle annular dark-field scanning transmission electron microscopy (AC HAADF-STEM) images further reveal the state of Fe atoms in f-Fe-NC. As shown in Figure 1F and Figure S4D, numerous tiny bright dots can be observed on the carbon matrix without aggregation, suggesting the atomic-level dispersion of Fe single atoms instead of aggregation.[29] The weight percentage of f-Fe-NC and Fe-NC are 0.57 wt.% and 0.79 wt.%, respectively, determined by the inductively coupled plasma optical emission spectroscopy (ICP–OES, Table S1).

The N_2 adsorption-desorption measurements were conducted to reveal Brunauer-Emmett-Teller (BET) specific surface area and pore distribution of each catalyst. As displayed in Figure S5A, the sharp increase at low relative pressure indicates the existence of abundant micropores in f-Fe-NC and Fe-NC. However, f-Fe-NC also exhibits a hysteresis loop at high relative pressure, which demonstrates the presence of ample mesopores induced by the evaporation of composite templates.[30] The BET surface areas are 523.67 m^2 g^{-1} and 692.07 m^2 g^{-1} for f-Fe-NC and Fe-NC (Table S2), respectively. The slight decrease of BET surface area of f-Fe-NC can be attributed to the collapse of micropores caused by strong interaction between ZnO and carbon matrix,[31] as revealed by its inferior adsorption capacity at low relative pressure. The pore distribution (Figure S5B) evidences that f-Fe-NC is hierarchically porous with micropores below 1.88 nm and mesopores ranging from 5 to 30 nm, while Fe-NC is micropore-dominated. The hierarchically porous structure of f-Fe-NC can provide enhanced capacity for mass transfer, which is evidenced by the water contact angle measurement (Figure S6). The lower water contact angle of f-Fe-NC (20.69°) suggests its superior permeability to electrolyte than Fe-NC (61.81°), which is beneficial for the formation of triple-phase reaction interface and mass transfer.[32]

Coordination environment for f-Fe-NC

To further understand the mechanistic role of composite templates during carbonization, X-ray photoelectron spectroscopy (XPS) was conducted. As illustrated in Figure S7, the atomic percentage of N and O are 4.78 at. % and 6.47 at. % in f-Fe-NC, respectively, lower than that of Fe-NC (5.90 at. % for O and 9.69 at. % for N), indicating that N and O are removed by composite templates during pyrolysis. The N 1s spectrum of f-Fe-NC and Fe-NC are deconvoluted into five sets of peaks, namely, pyridinic N, Fe-N, pyrrolic N, graphitic N and oxidized N,[33] respectively. As shown in Figure S8A&B, the content of pyridinic N in f-Fe-NC is significantly reduced, while the content of oxidized N is increased. Additionally, the O 1s spectrum of f-Fe-NC and Fe-NC show similar peaks of C=O (Figure S8C&D).[34] These changes indicate that pyridinic N and C=O are the main heteroatom species reacting with ZnO to form defective structures during the pyrolysis. Besides, as previously reported, C atoms can also react with ZnO to generate defect structures.[26,31,34]

The Raman spectra of f-Fe-NC and Fe-NC are shown in Figure S9. The D-band at 1350 cm^{-1} represents the defective carbon or disordered carbon resulted from heteroatoms-doping or topological carbon ring, while the G-band at 1580 cm^{-1} represents graphitic carbon.[35,36] The defect level can be identified with the radio of intensity of D-band and G-band (I_D/I_G), which are 0.99 for f-Fe-NC and 1.01 for Fe-NC, respectively. Noticeably, as revealed by ICP-OES (Table S1) and XPS (Figure S7), the contents of heteroatoms, such as N, O and Fe, are significantly decreased in f-Fe-NC, but there is only a slight difference between the values of I_D/I_G of two catalysts, indicating the abundance of defective carbon or topological carbon ring in f-Fe-NC. Aberra-

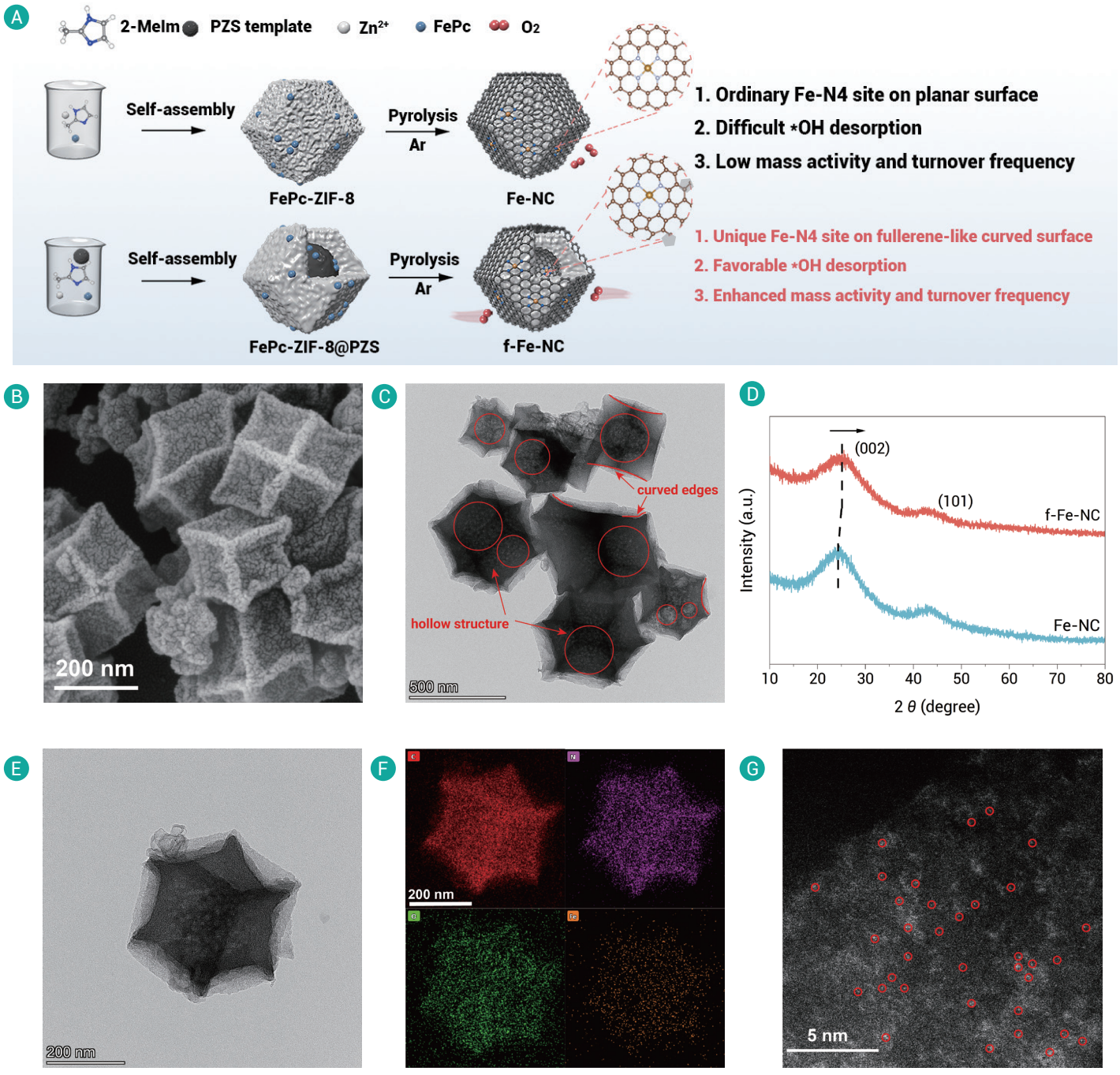

Figure 1. Schematic of the synthesis and structural characterizations of f-Fe-NC and Fe-NC (A)The synthesis process of f-Fe-NC and Fe-NC catalysts. (B) SEM image of f-Fe-NC. (C) TEM image of f-Fe-NC. (D) XRD patterns of f-Fe-NC and Fe-NC (E) STEM image and (F) corresponding EDS mapping of f-Fe-NC. (G) AC HADDF-STEM image of f-Fe-NC.

tion-corrected transmission electron microscopy (AC-TEM) measurement was conducted to further determine the species of D-band carbon species in f-Fe-NC. In Figure 2A, abundant carbon pentagons can be observed in AC-TEM image, indicating the co-existence of Fe-NC sites and carbon pentagons.[37] Notably, since the AC-TEM image is a projection of three-dimension structure in a two-dimension plane, and due to the presence of surface curvature, the observed hexagon and pentagon structures would undergo a certain deformation. Generally, in a planar carbon surface, the formation of carbon pentagon is accompanied by the formation of adjacent carbon defect,[38] as illustrated in Figure 2B, resulting in the existence of carbon vacancies and unpaired electrons. But surprisingly, in electron paramagnetic resonance (EPR) measurement (Figure S10), f-Fe-NC doesn't exhibit any signal intensity for vacancies or unpaired electrons, while Fe-NC shows an observable EPR peak, indicating the integrity of π-conjunction between carbon atoms in f-Fe-NC. This phenomenon indicates that the surface curvature caused by the inward collapse and lattice strain can trigger local atomic movement, thereby eliminating carbon vacancies and improve graphitization,[39] as illustrated in Figure 2B. Consequently, the carbon pentagons in f-Fe-NC are adjacent to five carbon hexagons thus forming fullerene-like curved surface with high graphitization and sp^2 hybridized carbon atoms without carbon vacancies and unpaired electrons.

The impact of fullerene-like curved surface on the coordination environment of f-Fe-NC is unveiled by the synchrotron-radiation-based X-ray absorption near-edge structure (XANES) and extended X-ray absorption fine structure (EXAFS) spectroscopy analyses. In the Fe K-edge XANES spectra (Figure 2C), the adsorption edge of f-Fe-NC and Fe-NC are located between FeO and Fe_2O_3, indicating oxide states of Fe in these samples are between +2 and +3. It is noteworthy that f-Fe-NC exhibits higher intensity of adsorption

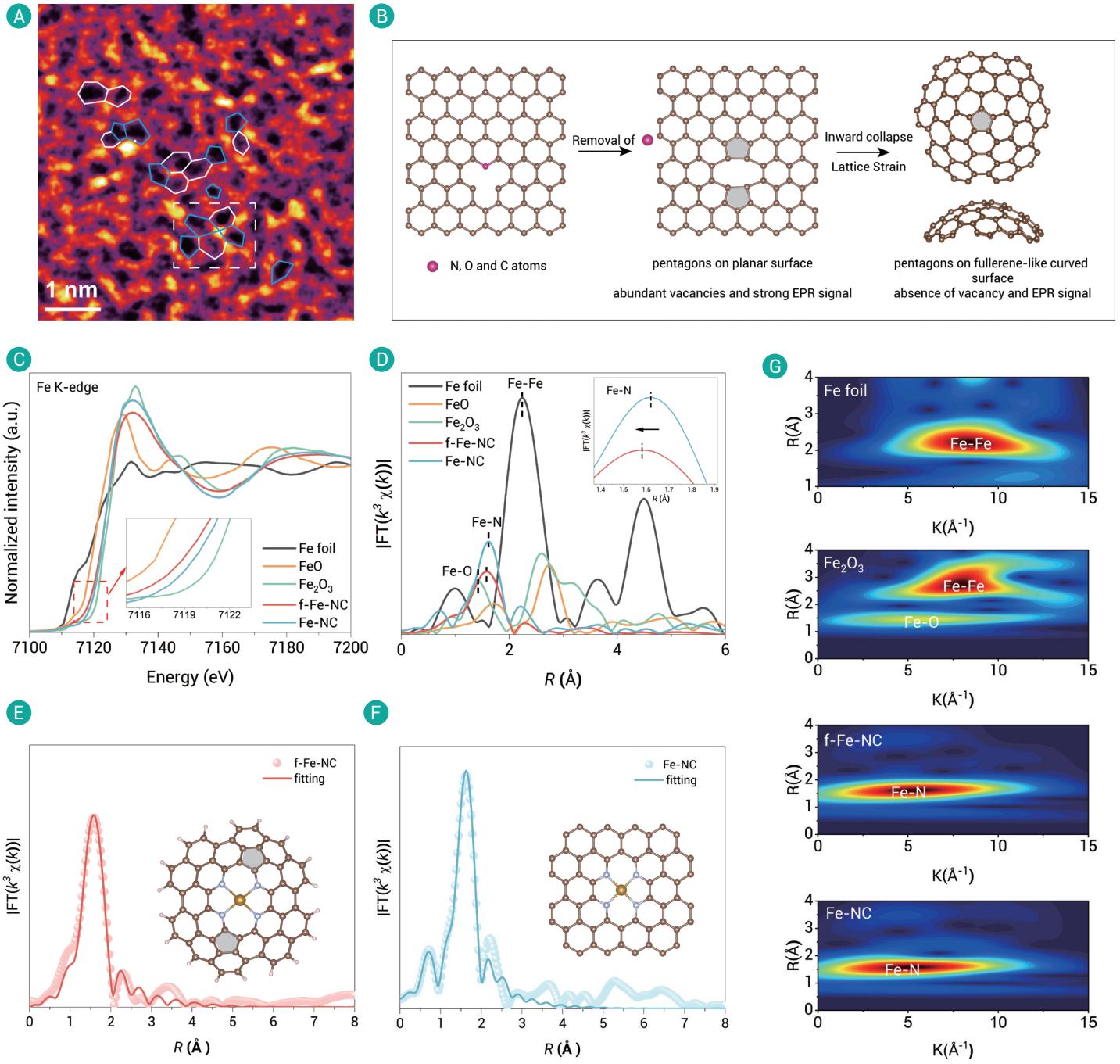

Figure 2. Coordination environment of f-Fe-NC and Fe-NC (A) AC-TEM image of f-Fe-NC. (B) Mechanism illustration of the formation of carbon pentagon and fullerene-like curved surface. Fe K-edge. (C) XANES spectra and (D) Fourier-transformed EXAFS spectra of Fe foil, FeO, Fe_2O_3, f-Fe-NC and Fe-NC. The EXAFS R-space fitting pattern of (E) f-Fe-NC and (F) Fe-NC. (G) WT contours of Fe foil, f-Fe-NC, Fe-NC and Fe_2O_3.

edge around 7119 eV than that of Fe-NC and the valence states of f-Fe-NC and Fe-NC derived from Fe K-edge XANES spectra are +2.37 and +2.41, respectively, as shown in Figure S11,which demonstrate the lower oxide state and rearranged electronic structure of Fe on the fullerene-like curved surface.[16,40,41] The Fourier-transformed EXAFS spectra of f-Fe-NC and Fe-NC along with other references are displayed in Figure 2D. The first-shell scattering peaks of f-Fe-NC and Fe-NC are located around 1.6 Å which are assigned to Fe-N path. Noticeably, the Fe-N peak of f-Fe-NC shifts negatively compared to that of Fe-NC, indicating the stretched Fe-N bonds on the curved surface of f-Fe-NC.[17] Besides, no peaks corresponding to Fe-Fe bond and Fe-O bond can be observed in EXAFS spectra of f-Fe-NC and Fe-NC, implying that the Fe atoms exist as single atoms rather than Fe particles, which is consistent with the XRD and AC-STEM results. The coordination environments of f-Fe-NC and Fe-NC are verified by conducting EXAFS fitting. The fitting curves and structural parameters show excellent consistency with experimental results as shown in Figures 2E&F and Table S3. The results of EXAFS fitting elucidate that the Fe single atom in f-Fe-NC is coordinated by 4 pyridinic nitrogen atoms on the curved surface with carbon pentagons adjacent to Fe-N_4 moiety, resulting in two sets of Fe-N bonds with different bond lengths, while the Fe atom in Fe-NC is embedded in the planar surface by 4 pyridinic nitrogen atoms with same Fe-N bonds. Compared to the Fe-N bonds in Fe-NC (2.04 Å), the Fe-N bonds in f-Fe-NC adjacent to carbon pentagons are shortened to 1.97 Å, while the other set is elongated to 2.07 Å, as shown in Table S3. These results demonstrate the regulating effect of fullerene-like curved surface on Fe-N_4 sites. Moreover, as shown in the wave transform (WT) contours of Fe K-edge EXAFS spectrum (Figure 2G), the

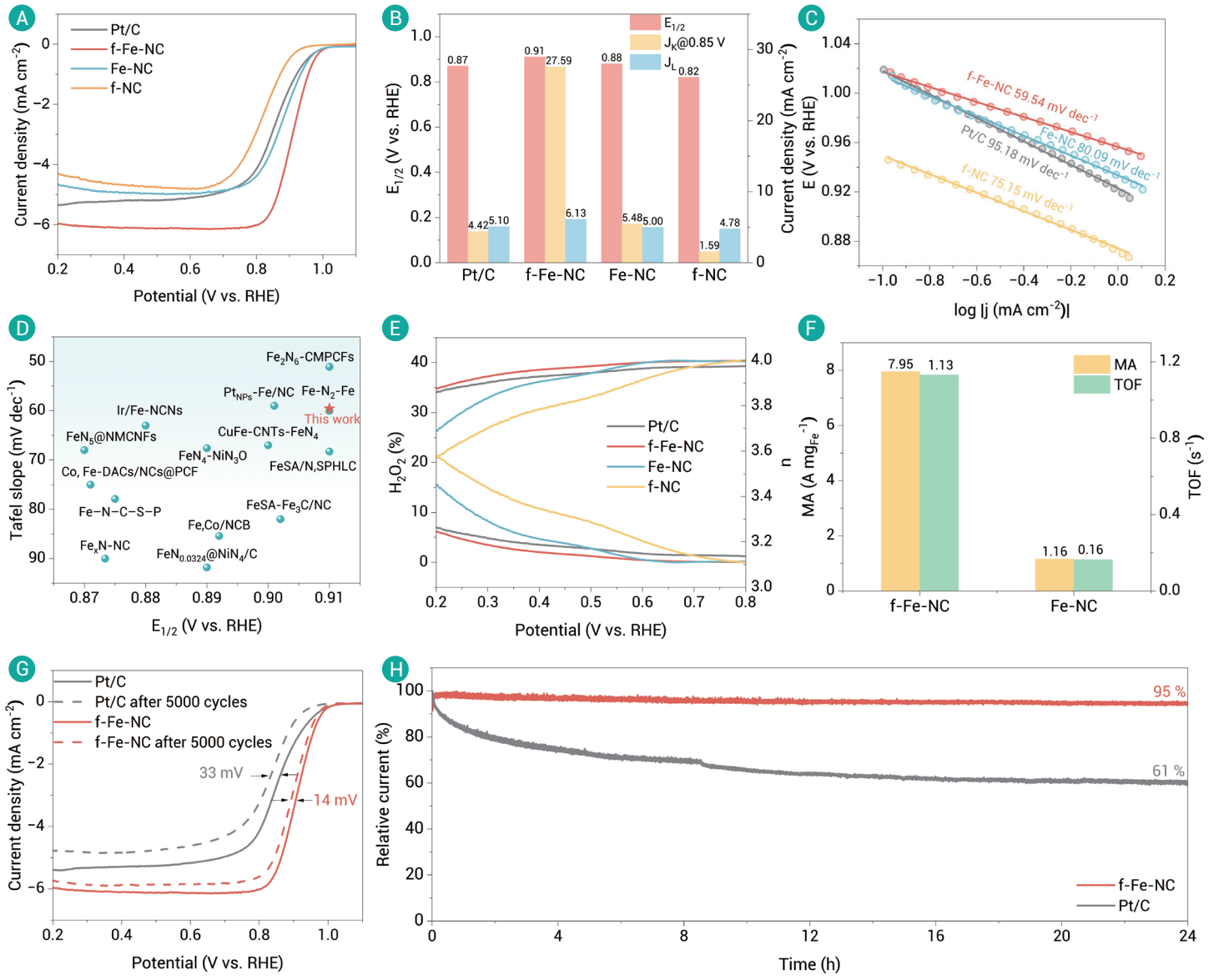

Figure 3. ORR performance in O_2-saturated 0.1 M KOH solution (A) ORR LSV polarization curves. (B) $E_{1/2}$, J_K@0.85 V and J_L. (C) Tafel slopes. (D) Comparison of f-Fe-NC and the state-of-art ORR catalysts. (E) Electron transfer number and H_2O_2 yield. (F) Mass activity and turnover frequency. (G) ORR LSV polarization curves before and after 5000 ADT cycles. (H) Long-term i-t test.

highest intensity of f-Fe-NC and Fe-NC exist around 5 Å, which corresponds to the Fe-N configuration, while the signals representing Fe-Fe and Fe-O path are absent in these plots. The WT contour results further validate the atomically dispersion of Fe atoms in both catalysts.

ORR performance

The electrocatalytic ORR performance of f-Fe-NC was evaluated by employing rotating disk electrode (RDE) measurements with a typical three-electrode system in O_2-saturated 0.1 M KOH solution. To achieve the optimal ORR performance of f-Fe-NC, synthesis conditions including the pyrolysis temperature and amounts of FePc were fully investigated, as shown in Figures S13-S14. In linear sweep voltammetry (LSV) curves (Figure 3A), f-Fe-NC displays the most positive onset potential (E_{onset}) of 1.003 V (unless further specified, all the potentials in this paper are referred to the reversible hydrogen electrode, RHE) and half-wave potential ($E_{1/2}$) of 0.91 V. The E_{onset} and $E_{1/2}$ of f-Fe-NC exceed those of the commercial Pt/C (E_{onset} = 0.996 V, $E_{1/2}$ = 0.87 V), Fe-NC (E_{onset} = 0.998 V, $E_{1/2}$ = 0.88 V) and f-NC (E_{onset} = 0.926 V, $E_{1/2}$ = 0.82 V), suggesting the enhanced intrinsic ORR activity of Fe-N_4 sites with adjacent pentagon defects. Notably, the E_{onset} and $E_{1/2}$ of f-NC are significantly lower than those of f-Fe-NC and Fe-NC, proving that the outstanding ORR performance of f-Fe-NC originates from the carbon pentagon modified-Fe-NC sites rather than the carbon pentagons. Additionally, f-Fe-NC reaches a limiting current density (J_L) of 6.13 mA cm^{-2} and a kinetic current density (J_k) of 27.59 mA cm^{-2} at 0.85 V, surpassing that of Pt/C (J_L = 5.10 mA cm^{-2}, J_k = 4.42 mA cm^{-2}), Fe-NC (J_L = 5.00 mA cm^{-2}, J_k = 5.48 mA cm^{-2}) and f-NC (J_L = 4.78 mA cm^{-2}, J_k = 1.59 mA cm^{-2}), as shown in Figure 3B. Additionally, the Tafel slope (Figure 3C) derived from polarization curves of f-Fe-NC (59.54 mV dec^{-1}) shows a smaller value than Pt/C (95.18 mV dec^{-1}), Fe-NC (80.09 mV dec^{-1}) and f-NC (75.15 mV dec^{-1}), signifying accelerated ORR kinetics of f-Fe-NC.[42] The outperforming intrinsic activity and rapid ORR kinetics of f-Fe-NC are also validated by the comparison with recently reported M-N-C catalysts (Figure 4D and Table S4).[43–57] On the other hand, according to the electron transfer number (n) calculated by rotating ring-disk electrode (RRDE) tests (Figure 4E) and Koutecky–Levich plots (Figure S15) derived from LSV curves at different rotating speeds (400 to 1600 rpm), the ORR process on f-Fe-NC follows a desirable 4e⁻ ORR pathway, through which the O_2 is reduced to H_2O instead of H_2O_2, thus achieving the maximum energy conversion efficiency. Moreover, f-Fe-NC possessed the lowest H_2O_2 yield (<6%) at 0.2 to 0.8V, further indicating the superior selectivity towards 4e⁻ ORR pathway of f-Fe-NC.

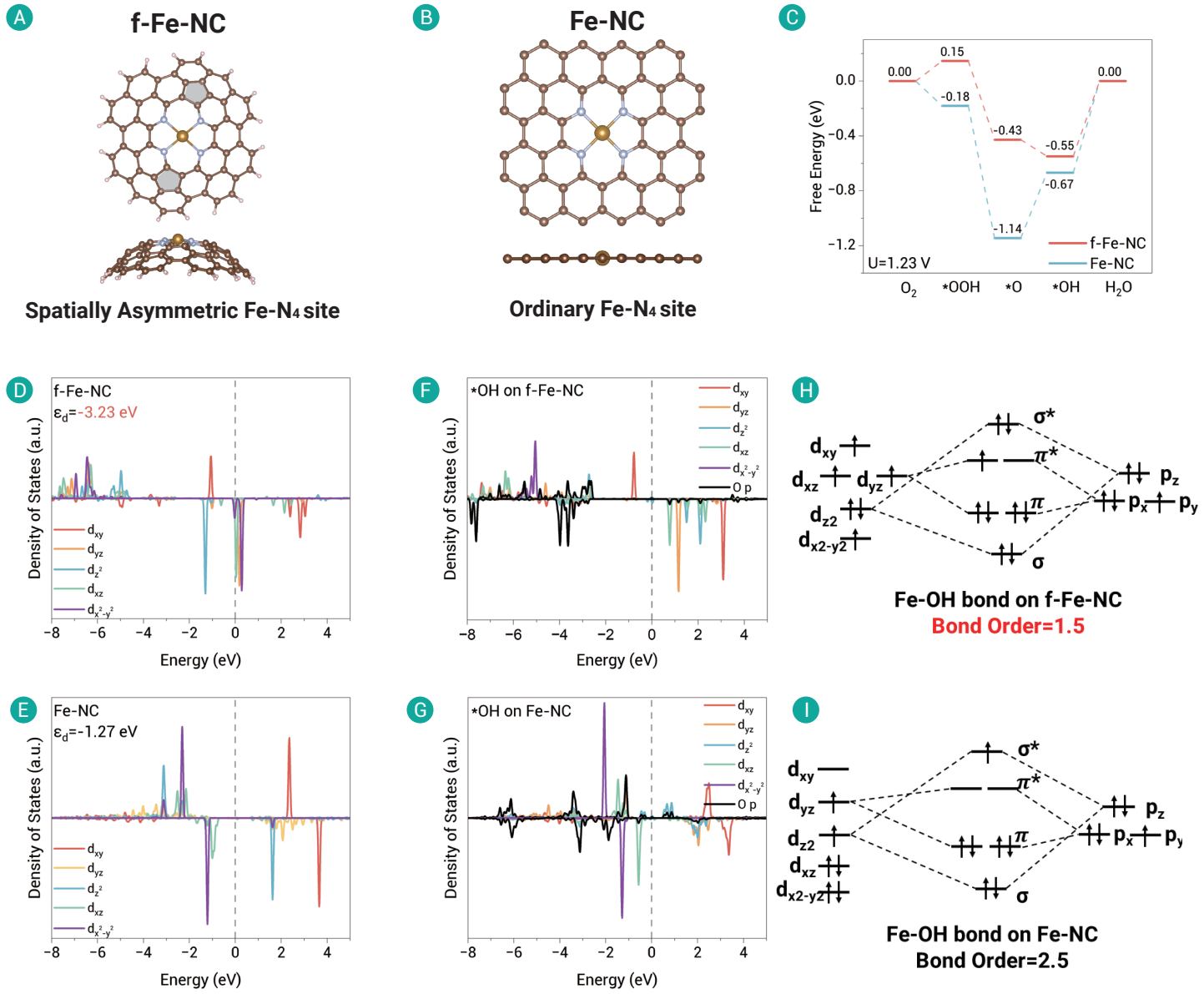

Figure 4. Theoretical calculations Optimized structures of (A) f-Fe-NC and (B) Fe-NC. (C) Free energy diagram at U = 1.23 V. Electronic density of stats (DOS) of Fe single atom of (D) f-Fe-NC and (E) Fe-NC. DOS of (f)f-Fe-NC-OH and (G) Fe-NC-OH. Molecular orbital configuration of Fe-OH bond on (H) f-Fe-NC and (I) Fe-NC.

The electrochemical double-layer capacitance (C_{dl}) is obtained by testing cyclic voltammetry (CV) curves of different scan rates ranging from 2 mV s^{-1} to 10 mV s^{-1} in non-Faraday range (Figures S16A&B). The calculated C_{dl} of f-Fe-NC is 30.15 mF cm^{-2}. Due to the decline of the micropore proportion in BET area, the C_{dl} of f-Fe-NC is inferior to that of Fe-NC (40.33 mF cm^{-2}). After normalizing the LSV curves by the ECSA values (Figure S17), the f-Fe-NC and Fe-NC show the same $E_{1/2}$ with Figure 3A, while the J_L of f-Fe-NC of f-Fe-NC is nearly 2 times higher than that of Fe-NC. This phenomenon suggests that the intrinsic activity of f-Fe-NC is superior to that of Fe-NC, despite lower ECSA values. The mass activity (MA) and turnover frequency (TOF) are estimated to further evaluate the intrinsic catalytic activity of f-Fe-NC.[58] As illustrated in Figure 3F, the MA of f-Fe-NC is 7.95 A mg_{Fe}^{-1}, which is around seven times that of Fe-NC (1.16 A mg_{Fe}^{-1}). Moreover, the TOF of f-Fe-NC (1.13 s^{-1}) is even one order of magnitude higher than that of Fe-NC (0.16 s^{-1}), despite Fe weight percentage (Table S1) of f-Fe-NC is lower than Fe-NC, indicating that the hierarchically porous structure is conducive to improving the atom utilization efficiency and site accessibility.[22] Furthermore, the acidic ORR activity of f-Fe-NC was tested in O_2-saturated 0.5 M H_2SO_4 solution. As shown in Figure S18 the f-Fe-NC exhibits an $E_{1/2}$ of 0.79 V, surpassing that of Fe-NC (0.76 V) and closing to that of commercial Pt/C (0.80 V). According to previous research,[59] the rate-limiting step in acidic ORR on Fe-N-C catalysts is the transfer and adsorption process of O_2. The enhanced ORR performance of f-Fe-NC further indicates that the oxygen transfer is highly accelerated by the hierarchically porous structure.

Apart from the catalytic activity, the stability is also an essential factor to evaluate the potential for practical applications of catalysts.[60] In the accelerated durability test (ADT, Figure 3G), f-Fe-NC shows remarkable stability with a minor $E_{1/2}$ loss of 14 mV after 5000 ADT cycles from 0.6 V to 1.0 V, much lower than Pt/C with a $E_{1/2}$ loss of 33 mV. In the long-term i-t chronoamperometric tests in O_2-saturated 0.1 M KOH solution at 0.6 V (Figure 3F), f-Fe-NC also displays the superior durability with a current retention rate of 95 % after 24 h, while the current density of Pt/C drops to 60 % rapidly. Furthermore, in the methanol tolerance measurement (Figure S19), no noticeable current decline occurs to f-Fe-NC after the methanol injection, while Pt/C exhibits a sharp deterioration in current density, indicating the excellent methanol resistance of f-Fe-NC. This robust performance suggests that f-Fe-NC could be a promising alternative to Pt/C in practical applications, by offering enhanced stability and efficiency under practical operating conditions.

Theoretical Computations

Density functional theory calculations were conducted to reveal the underlying mechanism for enhanced ORR performances on f-Fe-NC. The struc-

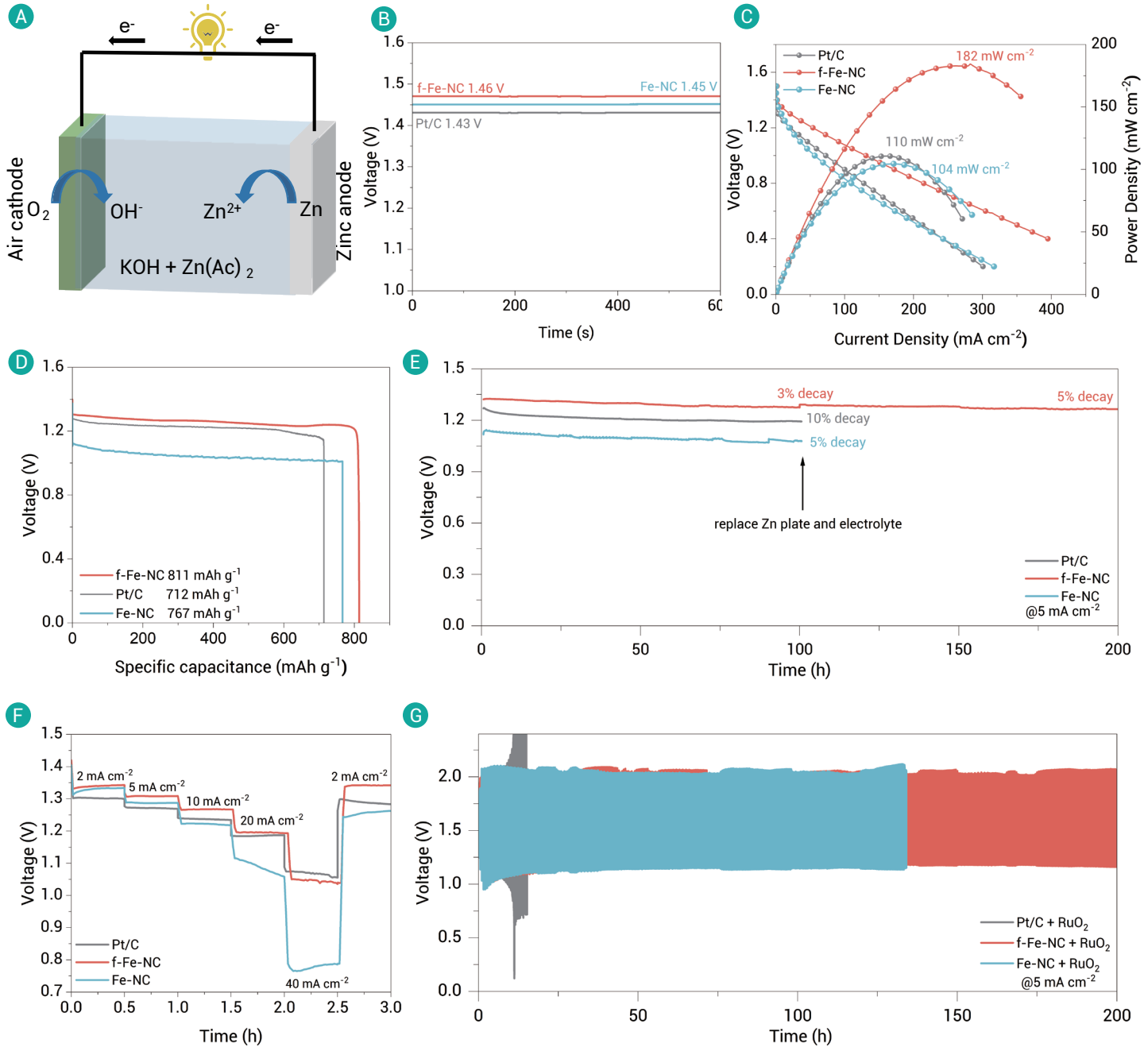

Figure 5. Performance of zinc-air battery (A) Schematic illustration of as-assembled zinc-air battery. (B) Open-circuit voltages. (C) Discharge polarization curves and power density. (D) Specific capacity at 10 mA cm^{-2}. (E) Long-term durability test at 5 mA cm^{-2}. (F) Discharge polarization curves at different current densities. (G) Charge-discharge curves at 5 mA cm^{-2}.

tures used for calculations were constructed according to the EXAFS fitting results. As shown in Figure 4A&B, the geometric structure of Fe-N_4 moiety in f-Fe-NC are stretched by fullerene-like curved surface, forming the spatially asymmetric Fe-N_4 coordination, while the Fe-N bonds in Fe-NC follow the ordinary square-planar pattern. The free energy diagram (Figure 4C) for ORR process was calculated to investigate the difference of intrinsic electrochemical activity between f-Fe-NC and Fe-NC. The optimized configurations of each step are shown in Figure S20-S21. The first step is the formation of *OOH intermediate, involving the adsorption of O_2 and hydrogenation. Under the equilibrium potential of ORR (U=1.23 V), the free energy changes (ΔG) are 0.15 eV on f-Fe-NC and -0.18 eV on Fe-NC. The increase in ΔG_1 indicates the weakened interaction between O_2 molecule and Fe single atom in f-Fe-NC, because of the two elongated Fe-N bonds. Subsequently, *O intermediate forms in the second hydrogenation process. While two catalysts both exhibit the decreased ΔG, the decline of f-Fe-NC is lower than that on Fe-NC, indicating the stronger interaction between Fe-NC and oxygenated intermediates. The last step is the desorption of *OH intermediate, which is the rate-determining step (RDS) for both catalysts. The ΔG_{max} is 0.55 eV for f-Fe-NC and 0.67 eV for Fe-NC, respectively, suggesting that the desorption of *OH is more efficient on f-Fe-NC than on Fe-NC. Similarly, the RDSs at U = 0 V and U = 0.9 V of both catalysts are also the desorption of *OH intermediate and f-Fe-NC exhibits lower ΔG_{max} than Fe-NC, as shown in Figures S22-23. The reduced ΔG_{max} accounts for the superior electrochemical performance of f-Fe-NC, and the enhanced *OH desorption is also in good agreement with the higher MA and TOF on f-Fe-NC. The excellent selectivity of $4e^-$ ORR pathway on f-Fe-NC is investigated at U = 0.7 V. As shown in Figure S24, the ΔG_{max} of $4e^-$ ORR pathway is only 0.02 eV, while that of $2e^-$ ORR pathway is 0.38 eV. The significant difference of ΔG_{max} indicates that despite the adsorption of *OOH is weakened on f-Fe-NC, f-Fe-NC is still more conducive to $4e^-$ ORR pathway.

To gain further insight into the facilitated *OH desorption on f-Fe-NC, the density of states (DOS) for f-Fe-NC and Fe-NC before and after the adsorption of *OH are investigated. As illustrated in Figures 4D&E, the electronic structure of f-Fe-NC is dramatically rearranged, with a significantly lower d-band center (ε_d=-3.23 eV) than that of Fe-NC (ε_d=-1.27 eV). According to the d-band center theory[61–63], d-band center is proportional to the binding strength. With the lower ε_d, the binding strength of Fe-OH bond is consequently weakened. According to the calculated DOS diagrams, the electronic structures of f-Fe-NC and Fe-NC are classified as d^6 configuration (left side of Figures 4H&I).[64] The atomic orbital of Fe-NC consists of fully occupied d_{x2-y2} and d_{xz} orbitals, half-occupied d_{z2} and d_{yz} orbital and an empty d_{xy} orbital. However, due to the geometric distortion of f-Fe-NC and declined d-band center, the electrons in f-Fe-NC are redistributed to lower energy levels, resulting in high-spin state Fe single atom with half-occupied d_{x2-y2}, d_{xz}, d_{yz} and d_{xy} orbitals and a fully occupied d_{z2} orbital.[65] As a result, the molecular orbital of Fe-OH bond undergoes a remarkable regulation. Figures 4F&G and Figures 4H&I show the DOS diagram of Fe-OH bond and the corresponding configuration of molecular orbitals on f-Fe-NC and Fe-NC, respectively. In both catalysts, the d_{z2} orbital of Fe is coupled with the p_z of O to form σ and σ* orbitals.[66] However, the σ* orbital of Fe-OH on f-Fe-NC is fully occupied and that of Fe-NC is half occupied. The π and π* orbitals of Fe-OH bond are composed of degenerate d_{xz} and d_{yz} orbitals of Fe and degenerate p_x and p_y orbitals of O. As a result, the π orbital is fully occupied and the π* orbital is occupied by one electron. The bond order of Fe-OH on f-Fe-NC is calculated to be 1.5. In terms of Fe-NC, the d_{xz} orbital is not involved in bonding, and the π* orbital is empty. The corresponding bond order is calculated to be 2.5, higher than that of f-Fe-NC (1.5). The degraded Fe-OH bond order on f-Fe-NC indicates the strength of bonding is drastically reduced,[58] which is in good consistency with the lower desorption free energy of f-Fe-NC. Moreover, the bond length of Fe-OH bond is calculated to be 1.85 Å on f-Fe-NC, while that of Fe-NC is 1.82 Å (Figure S20-S21). These phenomena suggest that the electronic structure rearrangement makes f-Fe-NC favorable for the desorption of *OH intermediate, thus facilitating the ORR performance and acquiring higher mass activity and turn over frequency.

Performance of zinc-air battery

To further evaluate the potential of f-Fe-NC for the practical application, aqueous Zinc-air battery (ZAB) was assembled, using f-Fe-NC as the cathode, 6.0 M KOH with 0.2 M $Zn(CH_3COOH)_2$ as the electrolyte and a polished zinc plate as the anode (Figure 5A). For comparison, 20 wt% Pt/C and Fe-NC were also used as cathodes to assemble ZABs. As displayed in Figure 5B and Figure S26-S27, f-Fe-NC-based ZAB exhibits a higher open-circuit voltage of 1.46 V than those of Pt/C and Fe-NC (1.43 V and 1.45 V, respectively). Additionally, the f-Fe-NC-based ZAB delivers a peak power density of 182 mW cm^{-2}, outperforming that of Pt/C-based ZAB (110 mW cm^{-2}), as shown in Figure 5C. Moreover, the f-Fe-NC-based ZAB possesses a specific capacity of 811 mAh g^{-1} at a current density of 10 mA cm^{-2}, while Pt/C and Fe-NC only exhibit specific capacities of 712 mAh g^{-1} and 767 mAh g^{-1}, respectively (Figure 5D). The performance of the f-Fe-NC-based ZAB also surpasses other recently reported ZABs based on M-N-C catalysts (Table S5). Furthermore, the f-Fe-NC-based ZAB demonstrates superior stability for 200 h with a voltage loss of mere 5% at 5 mA cm^{-1}, whereas the Pt/C-based and Fe-NC-based ZABs decay by 10% and 5% within 100 h, respectively (Figure 5E). In discharge polarization tests (Figure 5F), f-Fe-NC exhibits higher voltage at all current densities except 40 mA cm^{-2}, where the voltage of f-Fe-NC is only slightly lower than that of Pt/C. Moreover, the voltage of f-Fe-NC shows the best stability when the current density turns back to 2 mA cm^{-2}. In charge-discharge test, all the catalysts were mixed with equal amounts of RuO_2. As shown in Figure 5G, the f-Fe-NC-based ZAB can stably operate for 200h with lower charge voltage and higher discharge voltage than those of Pt/C and Fe-NC. In terms of practical applications, two f-Fe-NC-based ZABs in series can light up a LED light board, as shown in Figure S28. These results demonstrate the potential of f-Fe-NC in practical application.

CONCLUSION

In summary, Fe-N_4 sites on fullerene-like curved surface with adjacent carbon pentagons (f-Fe-NC) were synthesized by a composite template-assisted strategy. During the pyrolysis, the templates react fiercely with specific N, O and C atoms to generate carbon pentagons and evaporate to form hierarchically porous structures. Notably, carbon vacancies that would have been generated were eliminated by surface curvature, thus forming fullerene-like curved surface. Attributed to the Fe-N_4 site with high intrinsic ORR activity and hierarchically porous structure, f-Fe-NC achieves a competitive $E_{1/2}$ of 0.91 V with enhanced mass activity (MA) and turnover frequency (TOF). DFT calculations confirmed that the electronic structure of Fe-N_4 site was significantly regulated on fullerene-like curved surface, thereby facilitating the desorption of *OH intermediate. Aqueous zinc-air battery was subsequently assembled, which exhibited remarkable specific capacity and durability during long-term charge-discharge tests. Our study provides not only a new approach for the synthesis of carbon-based single atom catalysts with optimized active site and geometric structure, but also a deep insight into the formation of curved surface as well as the underlying mechanism of the impact of surface curvature on ORR performance.

REFERENCES

1. Liang J., Zhu Y., Yang H., et al. (2025). Structural design and active-site modulation of bifunctional electrocatalysts and electrolyte chemistry for zinc–air batteries. *Adv. Funct. Mater.* **35**:10535. DOI:10.1002/adfm.202510535
2. Lee J., Kim S.T., Cao R., et al. (2011). Metal–air batteries with high energy density: Li–air versus Zn–air. *Adv. Energy Mater.* **1**:34–50. DOI:10.1002/aenm.201000010
3. Chung H.T., Cullen D.A., Higgins D., et al. (2017). Direct atomic-level insight into the active sites of a high-performance PGM-free ORR catalyst. *Science* **357**:479–484. DOI:10.1126/science.aan2255
4. Cao P., Mu X., Chen F., et al. (2025). Breaking symmetry for better catalysis: insights into single-atom catalyst design. *Chem. Soc. Rev.* DOI:10.1039/D4CS01031K
5. Yu A. and Yang Y. (2025). Atomically dispersed metal catalysts for oxygen reduction reaction: Two-electron vs. four-electron pathways. *Angew. Chem. Int. Ed.* DOI:10.1002/anie.202424161
6. Xiong Y., Li H., Liu C., et al. (2022). Single-atom Fe catalysts for Fenton-like reactions: Roles of different N species. *Adv. Mater.* **34**:2110653. DOI:10.1002/adma.202110653
7. Hu X., Chen S., Chen L., et al. (2022). What is the real origin of the activity of Fe–N–C electrocatalysts in the O_2 reduction reaction. *J. Am. Chem. Soc.* **144**:18144–18152. DOI:10.1021/jacs.2c08743
8. Wang Y., Tang Y.-J. and Zhou K. (2019). Self-adjusting activity induced by intrinsic reaction intermediate in Fe–N–C single-atom catalysts. *J. Am. Chem. Soc.* **141**:14115–14119. DOI:10.1021/jacs.9b07712
9. Li Y., Luo X., Wei Z., et al. (2024). Precisely constructing charge-asymmetric dual-atom Fe sites for efficient oxygen reduction. *Energy Environ. Sci.* **17**:4646–4657. DOI:10.1039/D4EE01309C
10. Zhang D., She F., Chen J. and Li H. (2025). Why do weak-binding M–N–C single-atom catalysts possess anomalously high ORR activity? *J. Am. Chem. Soc.* DOI:10.1021/jacs.4c16733
11. Ji S., Mou Y., Liu H., et al. (2024). Manipulating electronic properties of Fe single atom catalyst via coordination engineering. *Adv. Mater.* **36**:2410121. DOI:10.1002/adma.202410121
12. Zhao T., Wang G., Xiao D., et al. (2025). Manipulating adjacent microenvironment of FeN_4 sites for efficient ORR. *ACS Catal.* **15**:1477–1486. DOI:10.1021/acscatal.4c06546
13. Zhou Q., Xue W., Cui X., et al. (2024). Oxygen-bridging Fe, Co dual-metal dimers boost reversible oxygen electrocatalysis. *Proc. Natl. Acad. Sci. U.S.A.* **121**:e2404013121. DOI:10.1073/pnas.2404013121
14. Zhang Z., Dai Y., Guo P., et al. (2024). Noncovalent assembly strategy for efficient synthesis of dual-atom catalysts. *Adv. Funct. Mater.* **34**:2407128. DOI:10.1002/adfm.202407128
15. Wang B., Yang X., Xie C., et al. (2024). A general metal ion recognition strategy to mediate dual-atomic-site catalysts. *J. Am. Chem. Soc.* **146**:24945–24955. DOI:10.1021/jacs.4c06173
16. Musgrave C.B., Su J., Xiong P., et al. (2025). Molecular strain accelerates electron transfer for enhanced oxygen reduction. *J. Am. Chem. Soc.* **147**:3786–3795. DOI:10.1021/jacs.4c16637
17. Zhao Y. (2025). Acidic oxygen reduction by single-atom Fe catalysts on curved supports. *Nature* **664**:668–675. DOI:10.1038/s41586-025-09364-6
18. Mao J., Iocozzia J., Huang J., et al. (2025). From lab-scale to industrialization: atomically M–N–C catalysts for ORR. *Energy Environ. Sci.* **11**:772–799. DOI:10.1039/C7EE03031B
19. Qiao M., Wang Y., Wang Q., et al. (2019). Hierarchically ordered porous carbon with FeN_4 for ORR. *Angew. Chem. Int. Ed.* **59**:2688–2694. DOI:10.1002/anie.201914123
20. Tan H., Tang J., Kim J., et al. (2019). Nanoporous Fe–N–C electrocatalysts for ORR. *J. Mater. Chem. A* **7**:1380–1393. DOI:10.1039/C8TA08870E
21. Peng L., Yang J., Yang Y., et al. (2022). Mesopore-rich Fe–N–C catalyst with FeN_4 sites. *Adv. Mater.* **34**:2202544. DOI:10.1002/adma.202202544

22. Xu Z., Xiao T., Li Y., et al. (2024). Effect of Schwarz P surface on ORR performance. *Adv. Mater.* **36**:2416204. DOI:10.1002/adma.202416204
23. Cui X., Jin R., Gao L., et al. (2025). High-loading single atoms via porous nanospheres for ORR. *Adv. Funct. Mater.* **35**:2510108. DOI:10.1002/adfm.202510108
24. Huang Y., Chen S., Li Y., et al. (2024). Flexible piezoelectric sensor based on PAN/MXene/ZnO composite. *Chem. Eng. J.* **488**:150997. DOI:10.1016/j.cej.2024.150997
25. Yan Y. (2025). General synthesis of neighboring dual-atomic sites. *Nat. Commun.* **16**:334. DOI:10.1038/s41467-024-55630-y
26. Wu Q., Jia Y., Liu Q., et al. (2022). Ultra-dense carbon defects as active ORR sites. *Chem* **8**:2715–2733. DOI:10.1016/j.chempr.2022.06.013
27. Tian H., Song A., Zhang P., et al. (2023). High durability Fe–N–C single-atom catalysts. *Adv. Mater.* **35**:2210714. DOI:10.1002/adma.202210714
28. Xia H., Pang R., Dong X., et al. (2023). Vacancy-coupling pentagons boosting ORR kinetics. *J. Am. Chem. Soc.* **145**:25695–25704. DOI:10.1021/jacs.3c08556
29. Liu S., Meyer Q., Jia C., et al. (2023). Degradation mechanisms of Fe–N–C catalysts. *Energy Environ. Sci.* **16**:3792–3802. DOI:10.1039/D3EE01166F
30. Li J., Xia W., Tang J., et al. (2022). MOF-derived graphene mesh for Fe–N_4 active sites. *J. Am. Chem. Soc.* **144**:9280–9291. DOI:10.1021/jacs.2c00719
31. Zhang P., Chen H.-C., Zhu H., et al. (2024). Inter-site structural heterogeneity in Fe catalysts. *Nat. Commun.* **15**:2062. DOI:10.1038/s41467-024-46389-3
32. Wu J. (2024). Structural engineering of Fe single-atom catalysts. *J. Energy Chem.* **98**:634–644. DOI:10.1016/j.jechem.2024.07.028
33. Guo W., Pan M., Xie Q., et al. (2025). pH-universal oxygen electrolysis via Fe catalysts. *Nat. Commun.* **16**:2920. DOI:10.1038/s41467-025-58297-1
34. Yu Y., Wang Y., Yang F., et al. (2024). Curved Fe–N_4 sites boosting ORR activity. *Angew. Chem. Int. Ed.* DOI:10.1002/anie.202415691
35. Zhang C., Shen W., Guo K., et al. (2023). Pentagonal defect-rich carbon electrocatalyst. *J. Am. Chem. Soc.* DOI:10.1021/jacs.3c00689
36. Yang J., Dai Q., Hou S., et al. (2025). Anti-self-discharge capability of Zn–halogen batteries. *Adv. Mater.* **37**:2418258. DOI:10.1002/adma.202418258
37. Zheng F., Zhang Y., Ding G., et al. (2024). Pentagon defects enabling sodium–sulfur batteries. *Adv. Funct. Mater.* **34**:2310598. DOI:10.1002/adfm.202310598
38. Ye G., Liu S., Zhao K. and He Z. (2023). Singlet oxygen induced etching boosting ORR. *Angew. Chem. Int. Ed.* **62**:e202303409. DOI:10.1002/anie.202303409
39. Wang Q., Lyu L., Hu X., et al. (2025). Surface curvature tuning Fe–N–C catalysts. *Angew. Chem. Int. Ed.* **64**:e202422920. DOI:10.1002/anie.202422920
40. Tang C., Jin R., Xia Y., et al. (2025). Asymmetric tailoring of Co single-atom catalysts. *Nano Energy* **137**:110776. DOI:10.1016/j.nanoen.2025.110776
41. Ma R., Tang C., Wang Y., et al. (2024). Electronic-state manipulation of polymers for ORR. *Angew. Chem. Int. Ed.* **63**:e202405594. DOI:10.1002/anie.202405594
42. Zhang S., Han Y., Zhang R., et al. (2024). Regulating Fe spin states for ORR. *Adv. Energy Mater.* **14**:2403899. DOI:10.1002/aenm.202403899
43. Liu M., Liu Y., Zhang X., et al. (2025). Axial Cl-mediated Fe–N–C catalysts. *Angew. Chem. Int. Ed.* DOI:10.1002/anie.202504923.
44. Xu Z., Zhu J., Shao J., et al. (2024). Anti-dissolving Fe_2N_6 sites for Zn–air batteries. *Energy Environ. Sci.* **17**:8722–8733. DOI:10.1039/D4EE03148B
45. Zhao S., Liu M., Qu Z., et al. (2024). Cascade synthesis of Fe–N_2–Fe dual-atom catalysts. *Angew. Chem. Int. Ed.* DOI:10.1002/anie.202408914.
46. Yuan M., Liu Y., Du Y., et al. (2024). Dual-shelled carbon support with asymmetric Fe sites. *Adv. Funct. Mater.* **34**:2401484. DOI:10.1002/adfm.202401484
47. Liu C., Yang R., Wang J., et al. (2025). Synergistic catalysts with Fe single atoms and Fe_3C clusters. *Angew. Chem. Int. Ed.* DOI:10.1002/anie.202501266.
48. Ma Q., Liao Y., Zhao Q., et al. (2025). PtNPs–Fe/NC catalyst for Zn–air batteries. *Small* **21**:2500344. DOI:10.1002/smll.202500344
49. Wu W., Hou Q., Huang T., et al. (2025). D-band modulation for efficient ORR. *Appl. Catal. B: Environ. Energy* **365**:124921. DOI:10.1016/j.apcatb.2024.124921
50. Wan Z., Ma Z., Deng X., et al. (2025). Weakening hydroxyl dissociation barrier in Fe–N–C catalysts. *Adv. Energy Mater.* DOI:10.1002/aenm.202501630.
51. Tian S., Chen L., Wu S., et al. (2025). FeN_4–NiN_3O diatomic catalysts for Zn–air batteries. *Chem. Eng. J.* **520**:166120. DOI:10.1016/j.cej.2025.166120
52. Liu Q., Chen J., Cao L., et al. (2025). Electronic communication between Ni and Fe–N species. *Adv. Funct. Mater.* **35**:2424597. DOI:10.1002/adfm.202424597
53. Pang H., Guo W., Ji X., et al. (2025). FeN_4 single atoms and Ir clusters synergy. *Chem. Eng. J.* **521**:166735. DOI:10.1016/j.cej.2025.166735
54. Zhao Y.-H., Ji Y.-R., Chen X.-Q., et al. (2025). Regulation of Fe coordination shells by S and P. *J. Colloid Interface Sci.* **688**:161–171. DOI:10.1016/j.jcis.2025.02.142
55. Wu S., Liu X., Mao H., et al. (2024). Tandem effect of nitrogen configuration promoting ORR. *Adv. Energy Mater.* **14**:2400183. DOI:10.1002/aenm.202400183
56. Lu Z., Wang Z., Yang Z., et al. (2025). Engineering CoN_4 and FeN_4 dual sites. *Adv. Funct. Mater.* **35**:2418489. DOI:10.1002/adfm.202418489
57. Chen L., Wang X., Lu T., et al. (2025). d-orbital spin polarization of Fe single atomic sites. *Appl. Catal. B: Environ. Energy* **366**:125007. DOI:10.1016/j.apcatb.2024.125007
58. Shen D., Sun F., Liang Z., et al. (2025). Axial-N induced Fe sites for ORR. *Angew. Chem. Int. Ed.* DOI:10.1002/anie.202505937.
59. Yu S., Levell Z., Jiang Z., et al. (2023). Rate-limiting step of ORR on Fe–N–C catalysts. *J. Am. Chem. Soc.* **145**:25352–25356. DOI:10.1021/jacs.3c09193
60. Zeng Y., Li C., Li B., et al. (2023). Breaking activity–stability trade-off of Fe–N–C catalysts. *Nat. Catal.* **6**:1215–1227. DOI:10.1038/s41929-023-01062-8
61. Zhao Z.-J., Liu S., Zha S., et al. (2019). Theory-guided design of catalytic materials. *Nat. Rev. Mater.* **4**:792–804. DOI:10.1038/s41578-019-0152-x
62. Liu B., Guo P., Dai Y., et al. (2025). Tailoring asymmetric atomic strain of FeN_4 sites. *Chem. Eng. J.* **507**:160174. DOI:10.1016/j.cej.2025.160174
63. Zhang Y.-L., Dai Y.-K., Liu B., et al. (2022). Atom–nanoparticle composite catalysts for Zn–air batteries. *J. Mater. Chem. A* **10**:3112–3121. DOI:10.1039/D1TA10559K
64. Liu K., Fu J., Lin Y., et al. (2022). Activity of Fe–N–C catalysts for ORR. *Nat. Commun.* **13**:2075. DOI:10.1038/s41467-022-29797-1
65. Yu M., Li A., Kan E. and Zhan C. (2024). Spin state evolution in Fe–N–C catalysis. *ACS Catal.* **14**:6816–6826. DOI:10.1021/acscatal.3c06122
66. Guo P., Liu B., Tu F., et al. (2024). Breaking Sabatier's vertex via dual active sites. *Energy Environ. Sci.* DOI:10.1039/D4EE00823E

FUNDING AND ACKNOWLEDGMENTS

The authors would like to thank the financial support from the Ministry of Science and Technology of the People's Republic of China (2022YFB4201802) and the Science and Technology Department of Jiangsu Province of China (BZ2024033, BT2024006). The modeling and calculations are supported by the Big Data Computing Center of Southeast University of China.

AUTHOR CONTRIBUTIONS

G.F. conceived the idea of this paper. S.H. performed the experiments, characterization and theoretical calculations. L.Y., K.Z. and Y.Z. helped with the RDE and ZAB testes. S.L. and H.Y. helped with the XAS characterization. Y.X. provided critical discussions to methodology. X.R. contributed to the funding acquisition, experimental resources and supervision of this research. All authors participated in the data analysis, writing and revising of this paper. All authors contributed to the manuscript and approved the final version.

DECLARATION OF INTERESTS

The authors declare no competing interests.

DATA AND CODE AVAILABILITY

Data are available from the corresponding author upon reasonable request.

SUPPLEMENTAL INFORMATION

It can be found online at: https://doi.org/10.59717/j.xinn-energy.2026.100154